A Single-Input Multioutput Capacitive Power Transfer System With Enhanced Misalignment Tolerance for UAV Swarm Charging

Xiaochen Zhang, Pan Sun, Enguo Rong, *Member, IEEE*, Gang Yang, Sisi Chang, and Qijun Deng

***Abstract*—This article proposes an electric field-coupled wireless charging system for Uncrewed Aerial Vehicle (UAV) swarms, capable of simultaneously charging multiple drones through a single transmitter-side setup while demonstrating excellent misalignment tolerance and load decoupling capability. First, a single-input multioutput electric field coupler with simple structure and superior structural adaptability is developed. Parameter optimizations are conducted to enhance misalignment tolerance, and its equivalent circuit model is established through finite element simulations. Second, an LCLC-CLL resonant network is designed to achieve constant current output, multiload decoupling, and transmitter-side load-adaptive zero-phase-angle operation. Finally, an experimental prototype is constructed to validate the theoretical analysis. Experimental findings demonstrate that the system attains a maximum single-load output power of 709.9 W with peak dc–dc efficiency reaching 89.06% . Stable power delivery is maintained across lateral misalignment ranges of [−125 mm, +125 mm] and rotational misalignment up to 240°. The system exhibits robust operational adaptability, sustaining high energy transfer efficiency during both load quantity variations and load imbalance scenarios. Furthermore, its advanced load-decoupling characteristics enable independent charging operation for multiple loads without cross interference, significantly enhancing the flexibility and cost-effectiveness of UAV swarm charging systems.**

***Index Terms*—Antimisalignment, capacitive power transfer (CPT), loads decoupling, single input multioutput (SIMO), uncrewed aerial vehicle swarm.**

I. Introduction

UNCREWED aerial vehicle (UAV) have become indispensable in modern applications ranging from aerial surveying [1], precision agriculture [2], logistics [3], disaster relief [4], and to military operations [5]. However, their operational endurance remains constrained by the inherent energy density limitations of current battery technologies.

Wireless power transfer (WPT) has demonstrated significant potential across various domains including electric vehicles [6], marine transportation [7], and consumer electronics [8]. Compared to conventional battery replacement or contact-based charging solutions, WPT-enabled UAV charging systems offer distinct advantages: 1) higher automation capability, and 2) elimination of connector wear losses. This technology presents a promising solution to overcome the persistent endurance limitations of battery-powered UAVs.

The design of efficient couplers constitutes a critical technical challenge in implementing WPT systems for UAV charging, a subject that has attracted significant research attention over the past decade [9]. Notably, in inductive power transfer (IPT) based UAV charging systems, four predominant coupler configurations have emerged as the mainstream solutions.

A. Conventional Planar Couplers

Standard planar circular/rectangular coils directly applied to UAVs [10], [11], [12], [13] suffer from poor structural compatibility, making them unsuitable for UAV wireless charging systems.

B. Modified Receiver Coil Couplers

Receiver coils redesigned according to UAV shapes are mounted on landing gears with ferrite cores to enhance coupling [14], [15], [16]. While demonstrating improved structural adaptability, these couplers involve complex design tradeoffs between coupling capability and misalignment tolerance.

C. Orthogonal Magnetic Field Couplers

Designed for UAVs with vertical rectangular landing gears, this configuration utilizes orthogonal magnetic fields to improve coupling performance [17], [18], [19], [20]. Compared to the aforementioned types, it shows advantages in structural compatibility, lightweight design, and rotational misalignment tolerance, though its coupling stability under lateral misalignment requires further optimization.

Received 19 April 2025; revised 11 July 2025; accepted 22 August 2025. Date of publication 28 August 2025; date of current version 13 November 2025. This work was supported by the Key Program of the National Natural Science Foundation of China under Grant U24A20144. Recommended for publication by Associate Editor K.-B. Park. *(Corresponding author: Pan Sun.)*

Xiaochen Zhang, Pan Sun, Gang Yang, and Sisi Chang are with the School of Electrical Engineering, Naval University of Engineering, Wuhan 430033, China (e-mail: d22380802@nue.edu.cn; 1007101026@nue.edu.cn; 1507111049@nue.edu.cn; m21181101@nue.edu.cn).

Enguo Rong is with the Department of Electrical Engineering, Kunming University of Science and Technology, Kunming 650500, China (e-mail: rong@kust.edu.cn).

Qijun Deng is with the School of Electrical Engineering and Automation, Wuhan University, Wuhan 430072, China (e-mail: dqj@whu.edu.cn).

Color versions of one or more figures in this article are available at https://doi.org/10.1109/TPEL.2025.3603638.

Digital Object Identifier 10.1109/TPEL.2025.3603638

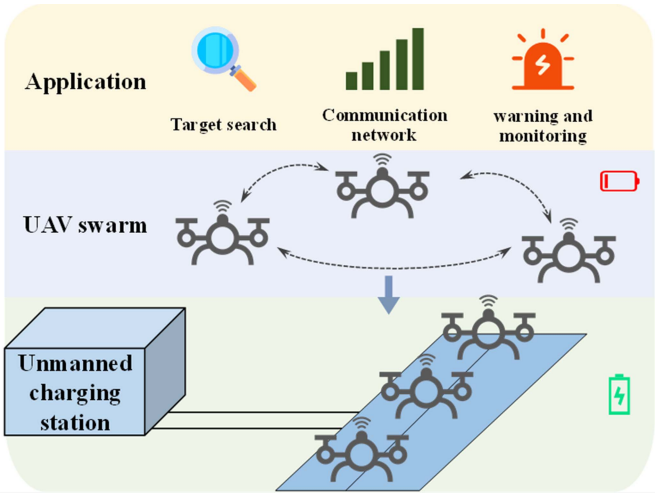

Fig. 1. Application of UAV swarm and wireless charging.

D. Array Transmitter Couplers

Multiple transmitter coils are employed to enhance misalignment tolerance [21], [22], [23]. While achieving strong positional adaptability, this approach necessitates UAV position detection and coil selection processes, significantly increasing operational complexity.

In summary, IPT technology remains constrained by structural complexity in coupler design, making it challenging to fully satisfy UAV wireless charging requirements. In contrast, capacitive power transfer (CPT) demonstrates inherent advantages including simplified coupler architecture, design flexibility, and reduced weight [24], [25]. These distinctive characteristics make CPT particularly suitable for UAV applications, prompting growing research interest in both domestic and international academic communities in recent years.

For instance, Muharam et al. [26] developed a point-type electric field coupler for quadcopter UAV, demonstrating strong structural adaptability and misalignment tolerance. However, its limited coupling capacitance resulted in low power transfer efficiency. Park et al. [27] proposed a protruding-platform coupler achieving 89.4% coupler efficiency with enhanced rotational misalignment tolerance, albeit at the expense of structural compatibility. Cai et al. [28] implemented an arrayed transmitter-plate coupler, where copper foil-wrapped cylindrical landing gears served as receiver plates, enabling 212 W power transfer at 500 kHz. Collectively, CPT couplers surpass IPT counterparts in installation flexibility and lightweight design.

Nevertheless, research on CPT-based UAV wireless charging remains limited. Moreover, current research on UAV wireless charging is predominantly limited to one-to-one charging configurations. As illustrated in Fig. 1, in practical applications such as target search [29], communication networking [30], and surveillance and alert systems [31], UAVs often operate in coordinated clusters. In such scenarios, the aforementioned one-to-one wireless charging methods fail to provide cost-effective solutions for concurrent multi-UAV charging.

To address the aforementioned challenges, this article proposes a capacitive wireless charging system for UAV swarms (UAVs-CWC). Through the joint design of couplers and resonant networks, the system achieves decoupled and simultaneous charging for multiple loads while maintaining excellent misalignment tolerance. The specific contributions are as follows.

1) A single-input multioutput (SIMO) coupler is proposed for UAV wireless charging, enabling simultaneous charging of multiple UAVs with a single transmitter excitation. This design offers advantages such as superior structural adaptability and lightweight construction.
2) An LCLC-CLL resonant network is proposed, along with its parameter design method, ensuring stable charging current and interplate voltage under varying load conditions and quantities, while achieving zero-phase-angle (ZPA) operation.
3) The proposed UAVs-CWC system demonstrates exceptional horizontal and rotational misalignment tolerance, as well as robust load decoupling capabilities.

TABLE I
MULTILOADS CPT TOPOLOGY

Topology	Characteristics	Applicable Scenarios
Domino	- Cascaded structure - Receiver of prior stage acts as transmitter for next	Highly specialized applications
MIMO	- Requires multiple inverters - Multiple transmitter-receiver plate pairs	High-power loads
SIMO	- Only one transmitter-side equipment required	Multiple low-power loads

II. SIMO Capacitive Coupler For UAVs Charging

A. SIMO Capacitive Coupler Design

The coupler functions as the critical interface enabling contactless energy transfer between the charging station and the UAV. Its design quality directly governs the system's charging speed and energy transfer efficiency. A well-designed wireless charging coupler for UAVs should exhibit good structural compatibility, lightweight characteristics, and misalignment tolerance [32].

As shown in Table I, capacitive couplers with domino topology [33], multiple-input multiple-output topology [34], and SIMO topology [35] can all realize the function of charging multiple loads simultaneously. Considering the relatively low charging power level of UAVs and giving full play to the transmission capacity of the inverter function, this article adopts the capacitive coupler with SIMO topology. The proposed UAVs-ECWC system topology is shown in Fig. 2. On the Transmitter transmitter side, a dc voltage source provides a stable input voltage (U_{dc}) as the energy supply. A high-frequency full-bridge inverter converts dc to ac, which is then injected into the coupler through the Transmitter-side resonant network. The coupler features a single input port and multiple output ports, enabling energy distribution from the transmitter to multiple receivers via electric field coupling. The received energy is subsequently

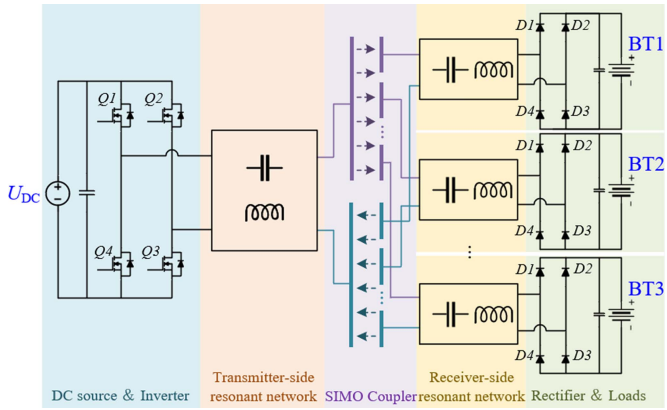

Fig. 2. Topology of UAVs-CWC system.

processed by receiver-side resonant networks and rectifiers to charge individual UAV batteries.

The UAVs-CWC system achieves simultaneous wireless charging for multiple UAVs using a single transmitter setup, significantly enhancing operational cost-effectiveness and deployment flexibility. This operational mode imposes special requirements on the electric-field coupler for SIMO configuration: The coupler should feature one input port and multiple output ports, enabling simultaneous power transfer from a single transmitter-side equipment to multiple UAVs, where the number of UAVs under charging can be dynamically adjusted according to operational demands. Subsequent SIMO coupler designs will be developed following these principles.

1) Transmitter Plates: As depicted in Fig. 2, the SIMO coupler's transmitter assembly comprises two metallic conductor plates connected to the two terminals of the transmitter-side resonant network, forming a closed power transfer loop. During wireless charging, these transmitter plates serve as the designated landing zone for UAVs, necessitating sufficient surface area to compensate for landing position inaccuracies and maximize the effective charging coverage. Fig. 3 illustrates two transmitter plate configurations.

a) *Monolithic Plate Design*: Features a unified structure with minimal conduction losses, ideal for deployment in spatially unconstrained environments.
b) *Distributed Plate Array*: Utilizes flexibly interconnected subplates with switchable connections, enabling space-efficient configurations and adaptive plate activation based on operational demands.

Both configurations demonstrate technical viability. For simplicity, this study adopts the monolithic plate design.

2) Receiver Plates: Three conventional installation positions exist for UAV wireless charging receivers: around the rotors of multirotor UAVs, beneath the UAV fuselage, and on the landing gear. CPT systems require only two receiver plates to form a power transfer circuit, offering advantages over IPT receivers in terms of lighter weight and flexible shape adaptability. However, the coupling capacitance of capacitive couplers is highly sensitive to the distance between the transmitter and receiver plates. Consequently, the area around UAV rotors is

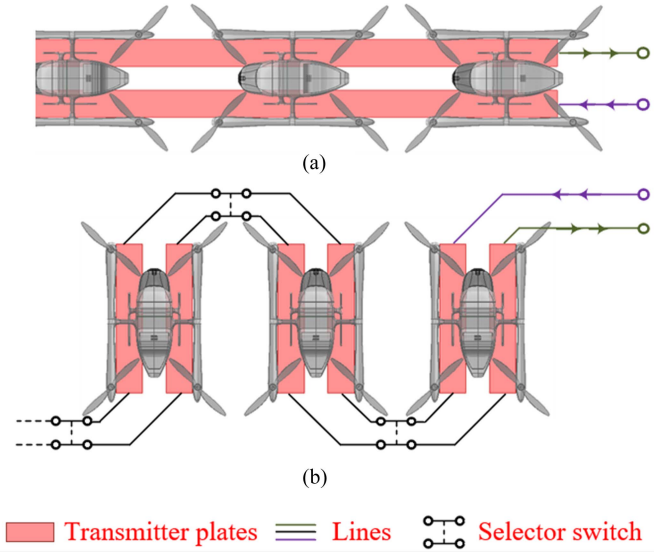

Fig. 3. Transmitter plate configurations. (a) Monolithic plate design. (b) Distributed plate array.

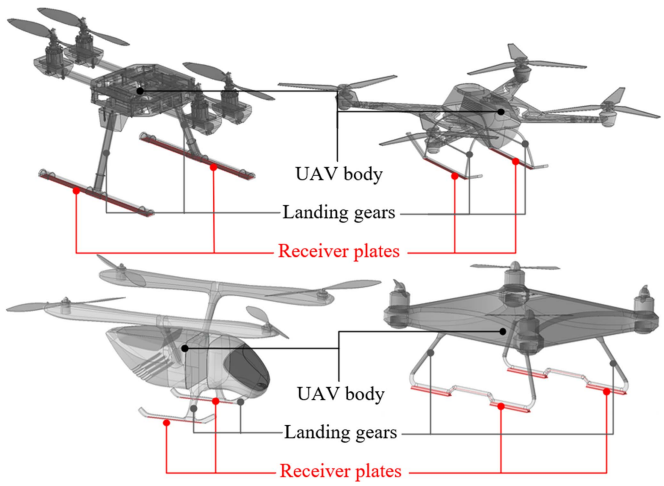

Fig. 4. Receiver plates mounted on landing gears of different UAV models.

unsuitable for receiver plate installation. Even when receiver plates are mounted beneath the UAV fuselage, protruding transmitter plates are required for effective energy transfer, which imposes stringent requirements on landing accuracy.

Considering the aforementioned factors, we installed the receiver plates on the bottom surfaces of UAV landing gears after implementing minor structural modifications. Fig. 4 demonstrates the installation method of the designed receiver plates on different UAV models. These UAVs share a common characteristic: their landing gears provide substantial projected contact area with the landing platform after touchdown, ensuring sufficient coupling capacitance formation in the electric field coupler.

3) Insulating Layer: The insulating layer is positioned between the transmitter and receiver plates, serving dual purposes of electrical insulation and acting as the dielectric medium to form the coupler's coupling capacitance. The selection of the

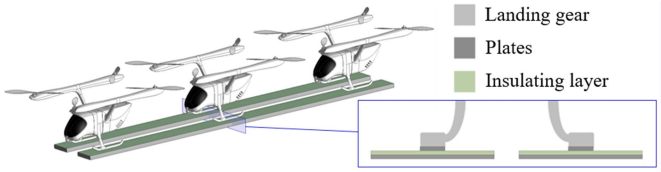

Fig. 5. Structure and installation of SIMO coupler.

insulating material directly affects the coupling capability and loss characteristics of the SIMO coupler. The coupling capacitance C_{coulp}between the transmitter and receiver plates can be approximated as

$$C_{\text{coulp}} = \frac{\varepsilon_0 \varepsilon_r A}{c} \tag{1}$$

where ε_0 is the vacuum permittivity, ε_r is the relative permittivity of the insulating layer, A represents the overlapping area of the plates, and c denotes the thickness of the insulating layer. Equation (1) indicates that materials with higher ε_r increase the coupling capacitance, thereby enhancing the system's power transfer capacity.

Concurrently, when the insulating layer is exposed to alternating electric fields between the plates, polarization losses occur due to the delayed polarization response relative to field variations. The power loss density is calculated by

$$P_{\text{unitV}} = \omega \varepsilon_0 \varepsilon_r \tan\delta \cdot E^2 \tag{2}$$

where ω is the angular frequency of the alternating electric field, $\tan\delta$ is the material's loss tangent, and $\tan\delta$ is the electric field strength.

After evaluating common electrical insulating materials—polyethylene, polypropylene, polyvinyl chloride (PVC), polytetrafluoroethylene, epoxy resin, ceramics, and mica—epoxy resin was selected for the insulating layer. This material offers high ε_r, excellent impact resistance, and the ability to reduce losses through doping modifications, making it highly suitable for SIMO coupler applications.

4) Overall Structure: The finalized SIMO coupler, as shown in Fig. 5, comprises metallic plates and an epoxy resin insulating layer. The transmitter plates are installed in the ground charging station, consisting of two identical sections connected to the two output terminals of the transmitter-side resonant network. These transmitter plates provide sufficient horizontal area to simultaneously accommodate multiple UAVs. The receiver plates are mounted on the bottom surfaces of UAV landing gears, featuring lightweight construction and excellent structural compatibility with UAV configurations without affecting flight performance.

B. Misalignment-Tolerance Coupler Parameter Optimization

This section presents the dimensional design and optimization of the SIMO electric field coupler to enhance its misalignment tolerance. Fig. 6(a) illustrates the structure and critical dimensions of the SIMO coupler in a planar view. Parameters l_{R1}, l_{R2}, and d_{R} are determined by the UAV landing gear configuration. For this study, $l_{\text{R1}} = 30$ mm, $l_{\text{R2}} = 300$ mm, $d_{\text{R}} = 270$ mm.

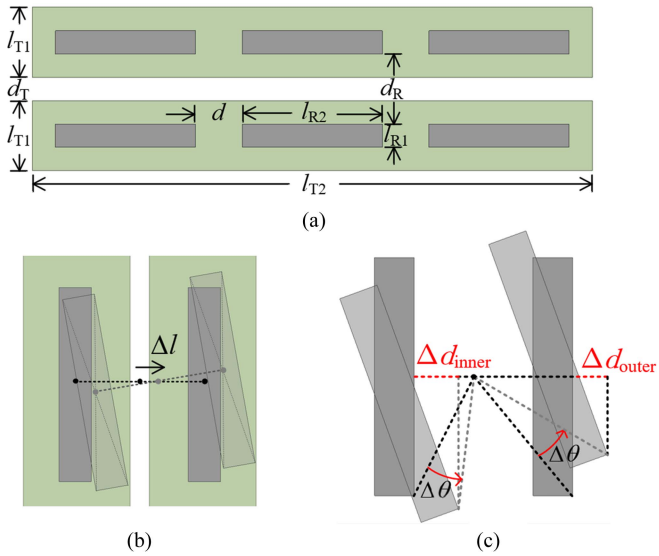

Fig. 6. Structure and dimensions of the SIMO electric field coupler. (a) Planar view. (b) Relative plate position changes under horizontal displacement (Δl) and rotational misalignment ($\Delta\theta$). (c) Detailed schematic of rotational misalignment.

Fig. 6(b) demonstrates the relative positional changes between the transmitter and receiver plates under UAV landing misalignments, including horizontal displacement (Δl), and rotational misalignment ($\Delta\theta$). Fig. 6(c) quantifies the endpoint displacement of the receiver plate caused solely by rotational misalignment. Here, Δd_{inner} represents the inward displacement of the receiver plate's innermost endpoint toward the center due to rotational misalignment, expressed as

$$\Delta\, d_{\text{inner}} = \frac{d_{\text{R}}}{2} - \frac{1}{2}\sqrt{d_{\text{R}}^2 + l_{\text{R2}}^2} \cdot \cos\left(\arctan\frac{l_{\text{R2}}}{d_{\text{R}}} + \Delta\theta\right). \tag{3}$$

Δd_{outer} denotes the outward displacement of the receiver plate's outermost endpoint from the center caused by rotational misalignment, as expressed in (4) shown at the bottom of this page.

When simultaneous Δl and $\Delta\theta$ occur, the combined effects must be considered. To ensure the receiver plate remains within the effective coupling area of the transmitter plates, the geometric constraints for l_{T1} (transmitter plate width) and d_{T} (transmitter plate spacing) must satisfy

$$\frac{d_{\text{R}} - d_{\text{T}}}{2} \geq \Delta l + \Delta d_{\text{inner}} \tag{5}$$

$$\frac{d_{\text{T}}}{2} + l_{\text{T1}} - \left(\frac{d_{\text{R}}}{2} + l_{\text{R1}}\right) \geq \Delta l + \Delta d_{\text{outer}}. \tag{6}$$

$$\Delta d_{\text{outer}} = \frac{1}{2}\sqrt{(d_{\text{R}} + 2l_{\text{R1}})^2 + l_{\text{R2}}^2} \cdot \cos\left(\arctan\frac{l_{\text{R2}}}{d_{\text{R}} + 2l_{\text{R1}}} - \Delta\theta\right) - \frac{d_{\text{R}}}{2} - l_{\text{R1}} \tag{4}$$

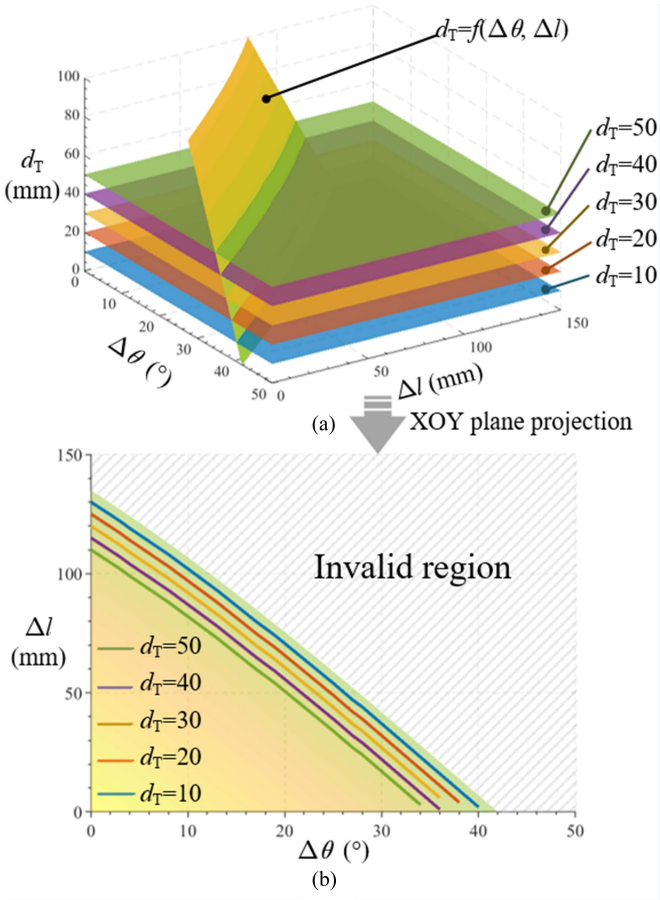

Fig. 7. Surface plot of d_T satisfying misalignment tolerance requirements under varying Δl and $\Delta\theta$. (a) Three-dimensional view. (b) Projection of the surface and intersection lines onto the *XOY* plane.

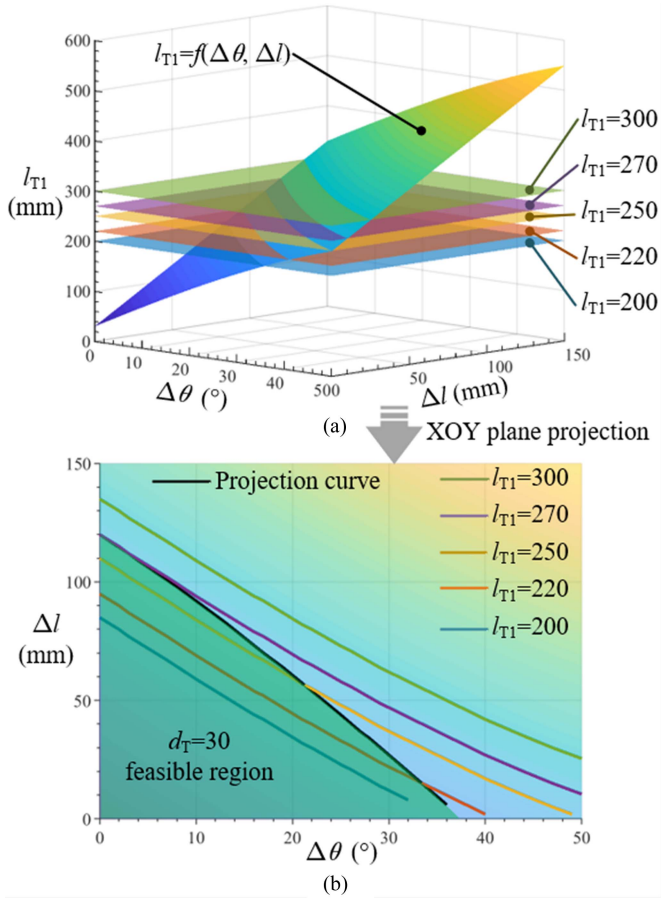

Fig. 8. Surface plot of l_{T1} satisfying misalignment tolerance requirements under varying Δl and $\Delta\theta$. (a) Three-dimensional view. (b) Projection of the surface and intersection lines onto the *XOY* plane.

First, optimize the transmitter plate spacing d_T. By setting (5) as an equality and substituting varying levels of Δl and $\Delta\theta$ into (3) and (5), the minimum d_T values satisfying misalignment tolerance requirements under different offset conditions are obtained, as shown in the three-dimensional (3-D) surface plot of Fig. 7(a). For practical implementation, the transmitter plates must not overlap ($d_T > 0$), so only the $d_T \in [0,\ 100\ \text{mm}]$ range of the $d_T = f(\Delta\theta, \Delta l)$ surface is plotted. Additionally, five planes ($d_T =\ 10,\ 20,\ 30,\ 40,\ 50$ m) intersect with the $d_T = f(\Delta\theta, \Delta l)$ surface. The intersection contours and the surface's projection onto the *XOY* plane are illustrated in Fig. 7(b).

Analysis of Fig. 7 indicates that the coupler's misalignment tolerance is limited, and a smaller d_T allows a larger allowable misalignment range. Considering the requirements to minimize C_{12} and ensure safe voltage withstand capability, d_T is selected as 30 mm.

Next, analyze the transmitter plate width l_{T1}. Similarly, substituting varying Δl and $\Delta\theta$ into (3)–(5) yields the l_{T1} dataset shown in Fig. 8(a). In Fig. 8(a), five planes ($l_{T1} = 200,\ 220,\ 250,\ 270,\ 300$ mm) intersect with the $l_{T1} = f(\Delta\theta, \Delta l)$ surface. The intersection contours and the surface's projection onto the *XOY* plane are presented in Fig. 8(b). The black solid line in Fig. 8(b) represents the projection of the intersection curve between $d_T = 30$ mm and $d_T = f(\Delta\theta, \Delta l)$ onto the *XOY* plane. The region bounded by this curve and the coordinate axes defines the misalignment tolerance range determined by $d_T = 30$ mm.

Analysis of Fig. 8 indicates that larger l_{T1} values allow greater receiver plate misalignment tolerance. However, since the overall misalignment tolerance is jointly governed by l_{T1} and d_T, increasing l_{T1} beyond 270 mm no longer enhances misalignment resilience. Consequently, l_{T1} is selected as 270 mm.

The transmitter plate length l_{T2} must satisfy (7) and (8), where N denotes the number of loads

$$d \geq 2\Delta l \tag{7}$$

$$l_{T2} \geq N \cdot d + N \cdot l_{R2}. \tag{8}$$

C. Equivalent Electric Circuit Model of SIMO Coupler

As shown in Fig. 9(a), a finite element analysis (FEA) model of the SIMO coupler was established in ANSYS Maxwell software. Both transmitter and receiver plates were modeled as aluminum, with the insulating layer material defined as FR4_epoxy. A sufficiently large solution domain was set to ensure the accuracy and convergence of the simulation results.

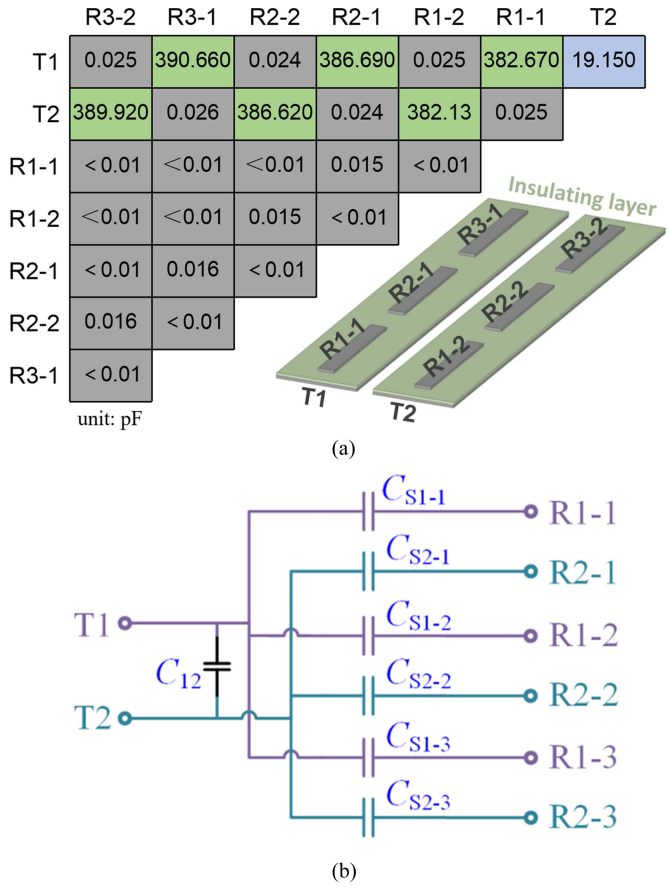

Fig. 9. (a) FEA model, capacitance. (b) Equivalent electric circuit model of SIMO coupler.

The ac conduction solver was selected to calculate the coupling capacitance between plates, with the solution frequency set to 500 kHz. The simulation results are summarized in the table within Fig. 9(a), where T1 and T2 are the transmitter plates, R1-*i* and R2-*i* are the receiver plates of the *i*th load ($i = 1,\ 2,\ 3$), and the numbers in the squares indicate the capacitance between the corresponding plates.

Analysis of the simulation results reveals that the capacitances between the transmitter plates and their corresponding receiver plates, as well as the capacitance between the two transmitter plates, are significantly larger than other stray capacitances. Therefore, stray capacitances can be neglected during circuit analysis, allowing the establishment of the SIMO coupler equivalent circuit model shown in Fig. 9(b). In this model, C_{12} represents the capacitance between transmitter plates T1 and T2, $C_{\mathrm{S1}-i}$ and $C_{\mathrm{S2}-i}$ denote the capacitances between the transmitter plates and the receiver plates of the *i*th load. The SIMO coupler is designed for scenarios where multiple UAVs are charged after landing. Due to the relatively tight coupling between the transmitter and receiver plates, the model remains effective unless the receiver plates are significantly displaced beyond the alignment range of the transmitter plates or overlap with two transmitter plates simultaneously.

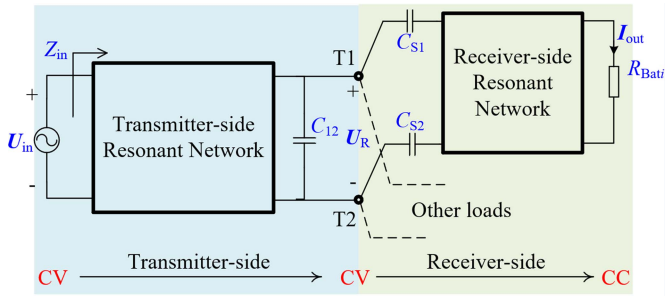

Fig. 10. Architecture of the SIMO CPT system.

III. Resonant Network Design and Characterization of SIMO CPT Systems

A. System Requirements Analysis for SIMO CPT Architecture

Fig. 10 illustrates the architecture of the SIMO CPT system, where $\boldsymbol{U}_{\mathrm{in}}$ represents the fundamental component of the inverter output voltage, Z_{in} denotes the system impedance, $\boldsymbol{U}_{\mathrm{R}}$ is the voltage between the transmitter plates, and R_{Bat} is the equivalent resistance of the UAV battery [36]. The objective of charging multiple UAVs simultaneously using a single transmitter imposes specific requirements on both the transmitter and receiver sides of the SIMO system.

Transmitter-Side Requirements: Constant transmitter plate voltage and load-adaptive ZPA. The multiple receiver sides connected in parallel to the transmitter plates necessitate stable transmitter plate voltage to achieve load decoupling and ensure independent charging for each UAV. During the charging process, the equivalent resistance R_{Bat} of the UAV battery varies dynamically, and the randomness of UAV charging introduces load switching events. The transmitter side must maintain ZPA under these operating conditions to improve energy transfer efficiency.

Receiver-Side Requirements: Current source behavior and load decoupling capability. The receiver side must exhibit constant current (CC) characteristics, maintaining stable output current despite variations in the equivalent resistance during UAV charging to meet fast-charging requirements. Additionally, decoupling between multiple loads is essential to ensure independent charging processes for each UAV without mutual interference.

B. Resonant Network Design and System Characterization

Based on the conclusions drawn in Section III-A, this section will separately design the resonant networks for the receiver and transmitter sides and present the fundamental characteristics of the system.

1) Receiver-Side CLL Network. CC Output and Purely Resistive: As shown in Fig. 10, all loads are connected in parallel with identical resonant network topologies. For simplicity, detailed analysis is performed for a single load, and the results can be generalized to other loads.

The equivalent circuit of a single load on the receiver side is shown in Fig. 11, where $Z_{\mathrm{R}i}$ represents the equivalent

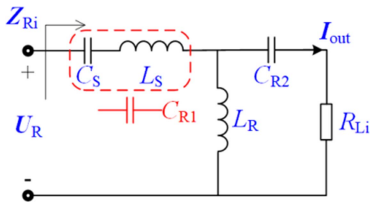

Fig. 11. Equivalent circuit of a single load on the receiver side.

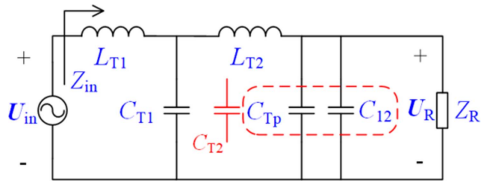

Fig. 12. Equivalent circuit on the transmitter side.

impedance of the receiver side for this load, C_S is the series equivalent capacitance of C_{S1} and C_{S2}, L_S and L_R are the resonant inductors, C_{R2} is the resonant capacitor, and R_{Li} denotes the equivalent ac resistance of the load

$$C_S = \frac{C_{S1}C_{S2}}{C_{S1}+C_{S2}}, \quad R_{Li} = \frac{8}{\pi^2} R_{Bati}. \tag{9}$$

C_S and L_S in series can be equivalent to the capacitance C_{R1}, i.e.,

$$C_{R1} = \frac{C_S}{1-\omega^2 L_S C_S}. \tag{10}$$

Then, $\boldsymbol{I}_{out}$ and Z_R can be expressed as

$$\boldsymbol{I}_{out} = \frac{jX_{LR}}{(R_{Li}-jX_{CR2})(jX_{LR}-jX_{CR1})-jX_{CR1}\cdot jX_{LR}}\boldsymbol{U}_R \tag{11}$$

$$Z_{Ri} = \frac{(R_{Li}-jX_{CR2})(jX_{LR}-jX_{CR1})+X_{CR1}X_{LR}}{R_{Li}+j(X_{LR}-X_{CR2})} \tag{12}$$

where $X_{CR1}=1/\omega C_{R1}$, $X_{CR2}=1/\omega C_{R2}$, $X_{LR}=\omega L_R$.

If the values of C_{R1}, L_R, and C_{R2} satisfy the formula

$$X_{CR1} = X_{CR2} = X_{LR}. \tag{13}$$

Then, (5) and (6) can be reduced to

$$\boldsymbol{I}_{out} = j\frac{\boldsymbol{U}_R}{X_{CR1}} \tag{14}$$

$$Z_{Ri} = \frac{X_{CR1}X_{LR}}{R_{Li}}. \tag{15}$$

2) Transmitter-Side LCLC Network. Constant Voltage Output and Load-Adaptive ZPA: Next, the resonant network on the transmitter side is designed. The fundamental equivalent circuit of the transmitter side is shown in Fig. 12, where L_{T1} and L_{T2} are the resonant inductors, C_{T1} and C_{Tp} are the resonant capacitors, $\boldsymbol{U}_{in}=2\sqrt{2}\boldsymbol{U}_{dc}/\pi$, and Z_R represents the equivalent impedance of the parallel-connected receiver sides, expressed as

$$Z_R = \frac{1}{\sum_{i=1}^{N}\frac{1}{Z_{Ri}}}. \tag{16}$$

C_{T2} is the parallel equivalent capacitance of C_{Tp} and C_{12}, i.e.,

$$C_{T2} = C_{Tp} + C_{12}. \tag{17}$$

L_{T1}, C_{T1}, and L_{T2} form a T-shaped network, then $\boldsymbol{U}_R$ and Z_{in} can be expressed as (18) and (19) shown at the bottom of this page, where $X_{CT1}=1/\omega C_{T1}$, $X_{CT2}=1/\omega C_{T2}$, $X_{LT1}=\omega L_{T1}$, $X_{LT2}=\omega L_{T2}$

If the values of L_{T1}, C_{T1}, L_{T2}, and C_{T2} satisfy

$$\begin{aligned} X_{LT1}X_{LT2}-X_{LT1}X_{CT1}-X_{LT2}X_{CT1}&=0\\ X_{LT2}-X_{CT2}-X_{CT1}&=0. \end{aligned} \tag{20}$$

Then, (18) and (19) can be reduced to

$$\boldsymbol{U}_R = -\frac{X_{LT2}}{X_{LT1}}\boldsymbol{U}_{in} = -\frac{X_{CT1}}{X_{CT2}}\boldsymbol{U}_{in} \tag{21}$$

$$Z_{in} = \frac{{X_{LT1}}^2}{{X_{LT2}}^2}Z_R = \frac{{X_{CT2}}^2}{{X_{CT1}}^2}Z_R. \tag{22}$$

3) Fundamental Characteristics of LCLC-CLL Topology SIMO CPT System: The fundamental equivalent circuit of the complete LCLC-CLL topology SIMO CPT system is illustrated in Fig. 13. It should be noted that the figure depicts only one receiver-side circuit in detail, which does not compromise the analytical accuracy.

Substituting (15) and (16) into (22), the input impedance expression of the system can be derived

$$Z_{in} = \frac{{X_{LT1}}^2}{{X_{LT2}}^2}\cdot\frac{1}{\sum_{i=1}^{N}\frac{R_{Li}}{X_{CR1}X_{LR}}} \tag{23}$$

where N is the total number of loads.

$$\boldsymbol{U}_R = \frac{-X_{CT1}\frac{Z_R\cdot -jX_{CT2}}{Z_R-jX_{CT2}}}{X_{LT1}X_{LT2}-X_{LT1}X_{CT1}-X_{LT2}X_{CT1}+(X_{LT1}-X_{CT1})\frac{Z_R\cdot -jX_{CT2}}{Z_R-jX_{CT2}}}\boldsymbol{U}_{in} \tag{18}$$

$$\begin{aligned} Z_{in} &= \frac{j\frac{Z_R\cdot -jX_{CT2}}{Z_R-jX_{CT2}}(X_{LT1}-X_{CT1})+X_{LT1}X_{CT1}+X_{LT2}X_{CT1}-X_{LT1}X_{LT2}}{\frac{Z_R\cdot -jX_{CT2}}{Z_R-jX_{CT2}}+jX_{LT2}-jX_{CT1}}\\ &= \frac{Z_RX_{CT2}(X_{LT1}-X_{CT1})+(X_{LT1}X_{CT1}+X_{LT2}X_{CT1}-X_{LT1}X_{LT2})Z_R-jX_{CT2}}{X_{LT2}X_{CT2}-X_{CT1}X_{CT2}+jZ_R(X_{LT2}-X_{CT2}-X_{CT1})}. \end{aligned} \tag{19}$$

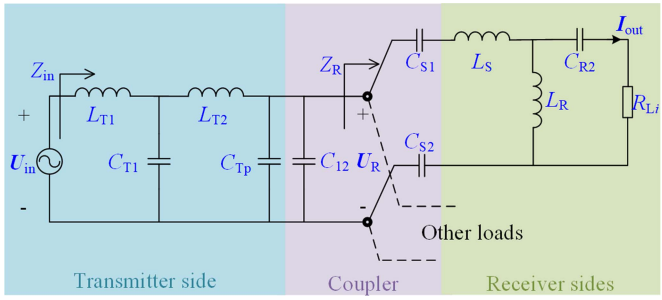

Fig. 13. Fundamental wave equivalent circuit of LCLC-CLL topology SIMO CPT system.

TABLE II
SIMO CPT SYSTEM PARAMETERS ($N = 3$)

Parameter (unit)	value	Parameter (unit)	value
l_{T1}(mm)	270	l_{T2}(mm)	1500
l_{R1}(mm)	30	l_{R2}(mm)	270
d_T(mm)	30	d_R(mm)	300
d(mm)	200	c(mm)	1
U_{DC}(V)	100	I_{out_DC}(A)	5
C_{12}(pF)	34.5	L_{T1}(uH)	10.88
C_{S1}(pF)	388	L_{T2}(uH)	54.41
C_{S2}(pF)	385	C_{T1}(nF)	11.17
C_S(pF)	193.25	C_{Tp}(nF)	2.2
L_S(uH)	588.83	C_{R2}(nF)	3.18
L_R(uH)	31.83	f(kHz)	500

Substituting (21) into (14), the expression for the load charging current can be obtained

$$\boldsymbol{I}_{\text{out}} = -j\frac{1}{X_{\text{CR1}}} \cdot \frac{X_{\text{LT2}}}{X_{\text{LT1}}}\boldsymbol{U}_{\text{in}}. \tag{24}$$

Through comprehensive analysis of (21), (23), and (24), the designed LCLC-CLL topology SIMO CPT system exhibits the following characteristics when satisfying resonance conditions (13) and (20).

1) *CC Output on Receiver Side*: The system provides stable charging current even when the equivalent resistance of lithium batteries varies during charging.
2) *Load-Adaptive ZPA on Transmitter Side*: The input impedance remains purely resistive regardless of load resistance variations or load quantity changes, effectively reducing reactive power and improving energy transfer efficiency.
3) *Constant Transmitter Plate Voltage*: Load decoupling is achieved, ensuring each load's charging process remains unaffected by other loads.

C. Integrated System Design Methodology

Fig. 14 illustrates the integrated design methodology for the UAVs-CWC system, with red numerals indicating the equation numbers referenced at each step. Table II presents the system parameters designed according to this methodology.

Specifically, the first step in system design is the design and modeling of the SIMO electric field coupler. At this stage, the structure and quantity of UAVs to be charged must be considered to determine the dimensions of the receiver plates and the configuration of the transmitter plates, as well as the material and thickness of the insulating layer. Based on this, the equivalent circuit parameters of the coupler (C_S and C_{12}) are obtained through FEA simulation.

Next, the circuit parameters of the system need to be designed. The input voltage $\boldsymbol{U}_{\text{in}}$, charging current $\boldsymbol{I}_{\text{out}}$, and operating frequency f are determined according to the UAV charging requirements and practical conditions. Then, L_{T1} and L_{T2} are tentatively selected based on experience, and L_{T1}, L_{T2}, and $\boldsymbol{U}_{\text{in}}$ are substituted into (15) to calculate the voltage between the transmitter plates $\boldsymbol{U}_R$ and other circuit parameters. After calculation, it is necessary to verify whether the obtained compensation parameters are practically feasible. If adjustments are needed, the values are revised and recalculated.

Finally, the misalignment tolerance of the coupler is optimized. The dimensions of the receiver plates (l_{R1}, l_{R2}, and d_R) determine the upper limit of the coupler's misalignment tolerance. Based on this, the optimized transmitter plate dimensions (l_{T1} and d_T) and the maximum misalignment range that maintain stable coupling capacitance can be determined. Combining this with the maximum number of charging loads N, the length of the transmitter plates is obtained (this study adopts monolithic transmitter plates).

IV. MULTILOAD PERFORMANCE ANALYSIS OF THE SYSTEM

A. Loss-Aware Efficiency Analysis for Multiload System

Energy transfer efficiency stands as one of the most critical performance metrics for wireless charging systems, necessitating the consideration of circuit component losses in its analysis. Fig. 15 illustrates the fundamental equivalent circuit of the multiload system incorporating component losses, where R_{LT1}, R_{LT2}, R_{LS}, and R_{LR} represent the internal resistances of resonant inductors, and R_{CS} denotes the equivalent resistance accounting for dielectric losses in the SIMO coupler's insulating layer under alternating electric fields. Analysis of Figs. 13 and 15 indicate that the former can be considered a special case of the latter when all loss factors are neglected. Thus, the energy transfer efficiency analysis can be developed based on the framework established in Section III-B.

Specifically, accounting for losses in receiver-side components. The term $-jX_{\text{CR1}}$ in (11) and (12) is replaced with $R_{\text{LS}} + R_{\text{CS}} - jX_{\text{CR1}}$, and jX_{LR} is substituted with $R_{\text{LR}} + jX_{\text{LR}}$. This yields the modified $\boldsymbol{I}_{\text{out}}$ expression (25), shown at the bottom of the next page, and $Z_{\text{R}i}$ (26), shown at the bottom of the next page. Similarly, for the transmitter side. The terms jX_{LT1} in (18) and (19) are replaced with $R_{\text{LT1}} + jX_{\text{LT1}}$, and jX_{LT2} is substituted with $R_{\text{LT2}} + jX_{\text{LT2}}$, resulting in (27) and (28), shown at the bottom of this page. By utilizing these four governing equations, the parameters Z_R, Z_{in}, $\boldsymbol{U}_R$, $\boldsymbol{I}_{\text{in}}$, and $\boldsymbol{I}_{\text{out}i}$ can be subsequently derived through sequential computation. This systematic approach ultimately enables the expression of

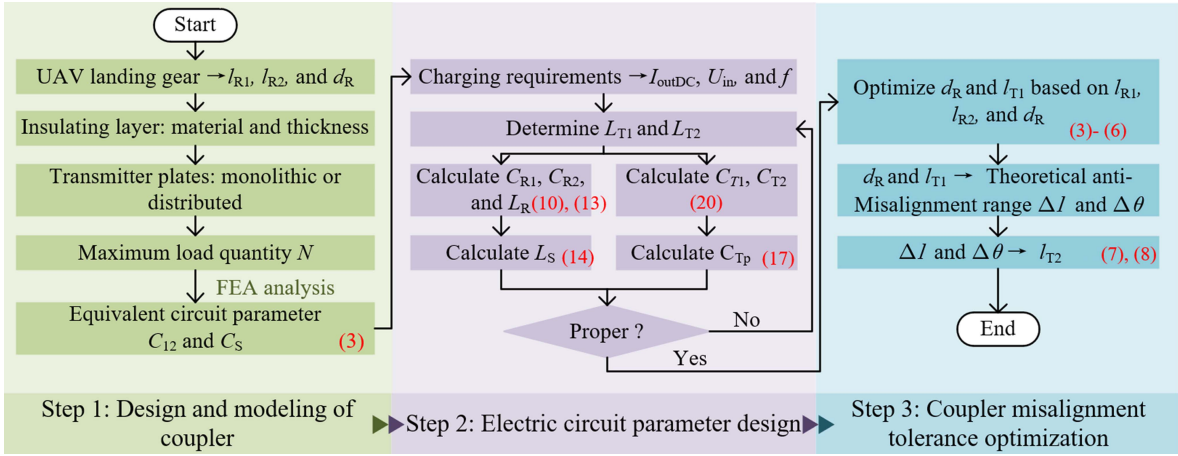

Fig. 14. Integrated design methodology for the UAVs-CWC system.

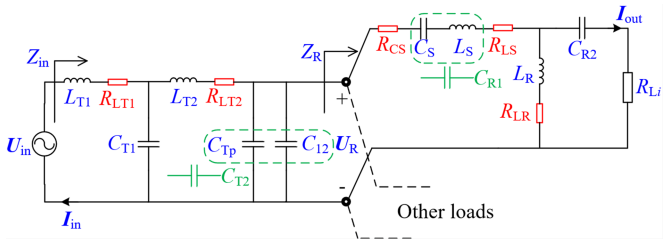

Fig. 15. Fundamental equivalent circuit of the multiload system incorporating component losses.

the multiload system efficiency as

$$\eta = \frac{\sum_{i=1}^{N} |\boldsymbol{I}_{\text{out}i}|^2 R_{\text{L}i}}{Re\left(\boldsymbol{U}_{\text{in}} \boldsymbol{I}_{\text{in}}^{*}\right)}. \tag{29}$$

It should be noted that the multiple load resistances $R_{\text{L}i}$ in (29) are not necessarily the same. In actual charging scenarios, when multiple loads use different types of batteries or are in different states of charge (SOC), their corresponding equivalent load resistances will differ, which is an unavoidable operating condition. A variable α is introduced to represent the load imbalance degree. Taking a three-load system as an example, the three loads can be R/α, R, and αR, respectively. A calculation program was written in MATLAB based on (25)–(29), where other parameters remain consistent with those in Table II, while the three load values are set to R/α, R, and αR to calculate the variation of key characteristic values of the system with α. The calculation results are shown in Fig. 16.

Analysis of Fig. 16 shows that load imbalance will affect the energy transfer efficiency of the system. As the load imbalance degree increases, although the total output power of the system increases, the energy transfer efficiency shows a downward trend. In addition, the load imbalance degree also affects the system impedance angle and transmitter plate voltage, but the impact is small under resonant operating conditions.

B. Simulation-Based Validation of Load Decoupling Capability

In UAV swarms, individual drones frequently operate at different SOC, necessitating staggered landing and departure times at charging stations. This requires the UAVs-CWC system to achieve effective interload decoupling, ensuring that the charging process of each UAV remains unaffected by other loads while simultaneously preventing interference with the charging of other drones.

$$\boldsymbol{I}_{\text{out}} = \frac{R_{\text{LR}} + jX_{\text{LR}}}{(R_{\text{L}i} - jX_{\text{CR2}})\left[R_{\text{LS}} + R_{\text{CS}} + R_{\text{LR}} + j\left(X_{\text{LR}} - X_{\text{CR1}}\right)\right] + \left(R_{\text{LS}} + R_{\text{CS}} - jX_{\text{CR1}}\right)\left(R_{\text{LR}} + jX_{\text{LR}}\right)} \boldsymbol{U}_{\text{R}} \tag{25}$$

$$Z_{\text{R}i} = \frac{(R_{\text{L}i} - jX_{\text{CR2}})\left[R_{\text{LS}} + R_{\text{CS}} + R_{\text{LR}} + j\left(X_{\text{LR}} - X_{\text{CR1}}\right)\right] + \left(R_{\text{LS}} + R_{\text{CS}} - jX_{\text{CR1}}\right)\left(R_{\text{LR}} + jX_{\text{LR}}\right)}{R_{\text{L}i} + R_{\text{LR}} + j\left(X_{\text{LR}} - X_{\text{CR2}}\right)} \tag{26}$$

$$\boldsymbol{U}_{\text{R}} = \frac{-X_{\text{CT1}}X_{\text{CT2}} - jX_{\text{CT1}}Z_{\text{R}}}{Z_{\text{R}} - jX_{\text{CT2}}\left\{\begin{array}{c}\left[\left(R_{\text{LT1}} + jX_{\text{LT1}}\right)\left(R_{\text{LT2}} + jX_{\text{LT2}}\right) + X_{\text{CT1}}\left(X_{\text{LT1}} + X_{\text{LT2}}\right) - jX_{\text{CT1}}\left(R_{\text{LT1}} + R_{\text{LT2}}\right)\right] \\ + \frac{(X_{\text{LT1}} - X_{\text{CT1}})X_{\text{CT2}}Z_{\text{R}} - jR_{\text{LT1}}X_{\text{CT2}}Z_{\text{R}}}{Z_{\text{R}} - jX_{\text{CT2}}}\end{array}\right\}} \boldsymbol{U}_{\text{in}} \tag{27}$$

$$Z_{\text{in}} = \frac{\frac{Z_{\text{R}}X_{\text{CT2}}(X_{\text{LT1}} - X_{\text{CT1}}) - jX_{\text{CT2}}Z_{\text{R}}R_{\text{LT1}}}{Z_{\text{R}} - jX_{\text{CT2}}} + \left[\begin{array}{c}\left(R_{\text{LT1}} + jX_{\text{LT1}}\right)\left(R_{\text{LT2}} + jX_{\text{LT2}}\right) + X_{\text{CT1}}\left(X_{\text{LT1}} + X_{\text{LT2}}\right) \\ -jX_{\text{CT1}}\left(R_{\text{LT1}} + R_{\text{LT2}}\right)\end{array}\right]}{\frac{Z_{\text{R}} \cdot -jX_{\text{CT2}}}{Z_{\text{R}} - jX_{\text{CT2}}} + R_{\text{LT2}} + j\left(X_{\text{LT2}} - X_{\text{CT1}}\right)}. \tag{28}$$

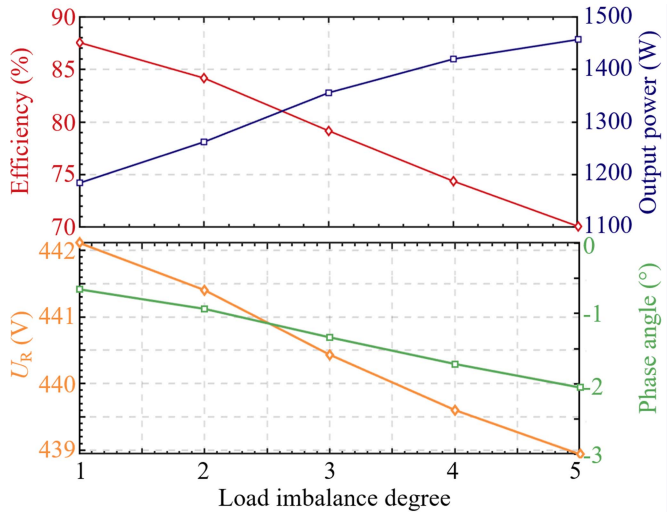

Fig. 16. Variations of (a) output power, efficiency, (b) impedance angle, and transmitter plate voltage of the multiload system with load imbalance degree.

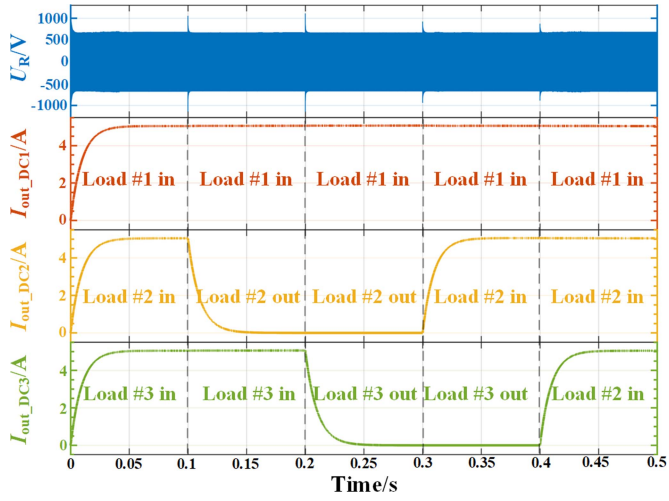

Fig. 17. Simulation waveforms of dynamic load switching.

To validate the load decoupling performance of the proposed UAVs-CWC system, a three-load circuit simulation model was implemented in MATLAB/Simulink based on the topology defined in Fig. 2 and the parameters detailed in Table II. The simulation protocol initiated with all three loads actively connected in the circuit. At 0.1 s simulation timestamp, Load #2 was intentionally disconnected from the network, followed by the controlled removal of Load #3 at 0.2 s. Subsequent system reconfiguration involved the deliberate reconnection of Load #2 at 0.3 s and the strategic reintegration of Load #3 at 0.4 s. Throughout the experimental sequence, the dynamic responses of both the rectified voltage $\boldsymbol{U}_{\mathrm{R}}$ and the output currents $I_{\mathrm{out\_dc}i}, (i = 1, 2, 3)$ were continuously monitored, with their temporal waveforms systematically documented and graphically represented in Fig. 17.

As clearly demonstrated in Fig. 17, $\boldsymbol{U}_{\mathrm{R}}$ maintains exceptional stability regardless of dynamic variations in the quantity of

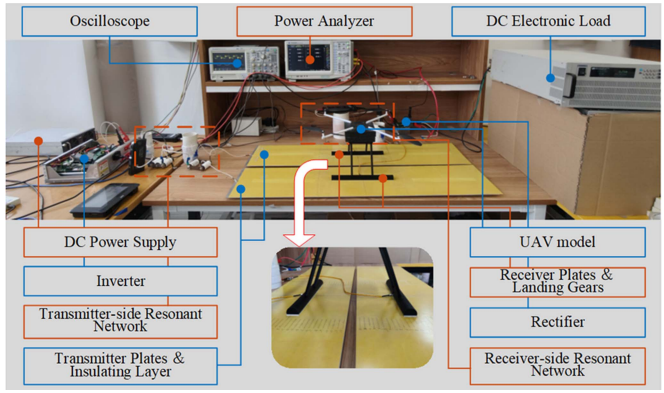

Fig. 18. Single-load prototype system.

TABLE III
EXPERIMENT SYSTEM PARAMETERS

Parameters (unit)	Designed value	Actual value	Parameters (unit)	Designed value	Actual value
C_{12}(pF)	34.5	33	L_{T1}(uH)	10.88	10.7
C_{S1}(pF)	388	326	L_{T2}(uH)	54.41	50.7
C_{S2}(pF)	385	337	C_{T1}(nF)	11.17	10.2
C_{S}(pF)	193.25	165.7	C_{Tp}(nF)	2.2	2.03
L_{S}(uH)	588.83	580.98	C_{R2}(nF)	3.18	3.32
L_{R}(uH)	31.83	30.47	f(kHz)	500	499.8

charging loads. Particularly noteworthy is the observed characteristic that the charging current of Load #1 remains unaffected by the sequential connection/disconnection operations of Loads #2 and #3. This empirical evidence conclusively verifies the independent charging operation of individual loads, with the UAVs-CWC system successfully attaining effective load decoupling through its innovative topological configuration.

V. Simulation and Experimental Verification

A. Experimental Platform

A single-load prototype system, as shown in Fig. 18, was first constructed. The prototype consists of a dc power supply (INFY POWER REG75035), a SiC MOSFET (Infineon IMZ120R045M1XKSA1)-based full-bridge inverter, a transmitter-side resonant network (L_{T1}, L_{T2}, C_{T1}, and C_{Tp}), two aluminum transmitter plates, two epoxy resin insulating boards, two aluminum receiver plates mounted on a UAV mockup, a receiver-side resonant network (L_{S}, L_{R}, and C_{R2}), a SiC Schottky barrier diodes (Wolfspeed C4D20120D)-based rectifier, and a programmable electronic load (ITECH IT8900A). The resonant capacitors employ film capacitors with superior high-frequency characteristics, while the resonant inductors are air-core designs consisting of PVC cylinders wound with Litz wire. Power analyzers (ZLG PA5000H) and oscilloscopes (ZLG ZDS3024 Plus) were used to measure power parameters and observe waveforms during experiments.

The parameters of the experimental prototype are listed in Table III. It should be noted that discrepancies exist between the designed and actual values of certain parameters. This arises

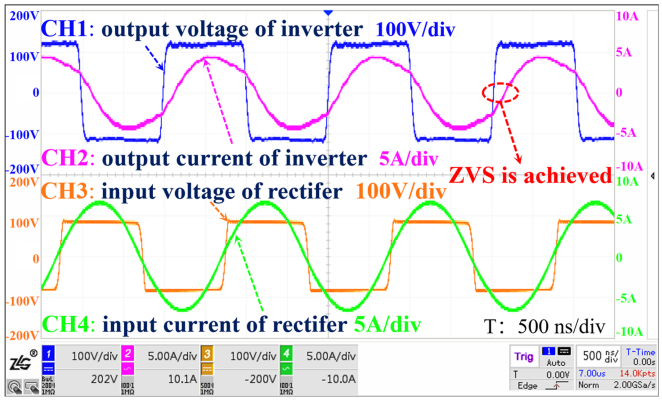

(a)

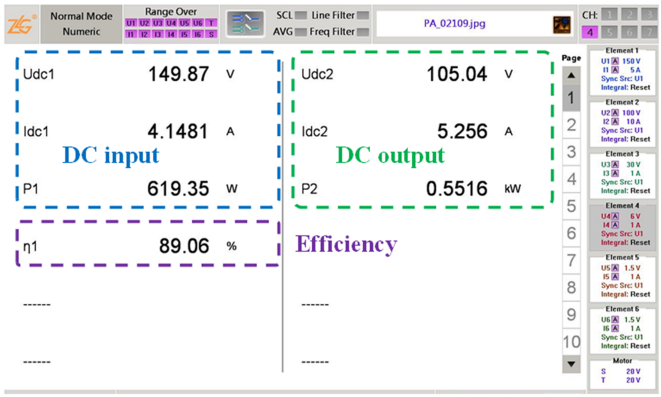

(b)

Fig. 19. System waveforms and power/efficiency metrics. (a) AC waveforms of inverter output and rectifier input under steady-state operation. (b) Power and efficiency at rated output capacity.

from two factors: air gaps between the plates and insulating layers in the fabricated SIMO coupler, which result in measured C_{S1} and C_{S2} values being lower than simulated values under identical dimensions, and intentional slight detuning of certain inductors from their resonant values to achieve zero-voltage switching (ZVS) for reduced inverter losses, thereby making the input impedance Z_{in} weakly inductive.

B. Power Transfer Capability Test

To evaluate the power transfer capability and efficiency of the UAV wireless charging system, power transfer capability tests were first conducted. The system's operational waveforms and power/efficiency metrics during stable operation are depicted in Fig. 19. Fig. 19(a) displays the ac voltage and current waveforms of both the inverter and rectifier under steady-state conditions. The sinusoidal inverter output current exhibits a smooth profile with slight phase lag relative to the voltage waveform, confirming successful ZVS implementation. Fig. 19(b) quantifies the system's power transfer performance at rated capacity, demonstrating a dc output power of 551.6 W with 89.06% dc–dc efficiency. These metrics represent state-of-the-art performance levels among contemporary CPT-based wireless charging systems for UAV applications.

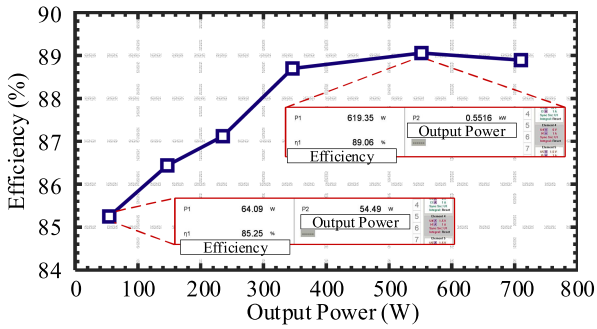

Fig. 20. Efficiency versus output power.

The energy transfer efficiency was measured at different output power levels, and the power-efficiency curve is plotted in Fig. 20. The system delivers an adjustable output power ranging from 54.49 W to 709.9 W, capable of meeting the charging requirements of various UAV models. The efficiency remains above 85% across the entire power range, peaking at 89.06% .

C. Misalignment Tolerance Validation

Misalignment tolerance stands as a critical performance metric for UAV wireless charging systems. This capability was evaluated through both open-loop prototype experiments and finite element-circuit cosimulations to validate the misalignment resilience of the proposed UAVs-CWC system.

It should be clarified that, as shown in Fig. 18, the transmitter plates provide ample spatial allowance along their longitudinal axis. Consequently, the system inherently demonstrates superior horizontal misalignment tolerance along this direction, which is not explicitly tested. Experimental investigations focused exclusively on horizontal misalignment along the transmitter plates' transverse axis.

Regarding rotational misalignment, the central symmetry of the plate geometry and the nonpolar configuration of the receiver plates ensure that rotational misalignment performance within the $[0, 90°]$ range is universally applicable to the full 360° circumferential scope.

1) Horizontal Misalignment: The UAV was displaced along the transverse axis of the transmitter plates while recording variations in system output power and efficiency. Concurrent cosimulations in ANSYS Maxwell and MATLAB/Simulink replicated this process to track simulated power variations. Experimental and simulated results were normalized and collectively presented in Fig. 21(a). It demonstrates that when the receiver plate remains within the effective coupling region, the experimental results exhibit complete agreement with theoretical analyses, maintaining stable wireless charging performance. Using a 10% output power deviation threshold, the experimentally validated horizontal misalignment tolerance range is $[-125\ \text{mm}, 125\ \text{mm}]$.

2) Rotational Misalignment: Similarly, Fig. 21(b) presents experimental and simulated results for rotational misalignment in a quarter circle. The data indicates that when $\Delta\theta \leq 40°$, the receiver plate remains within the effective coupling region

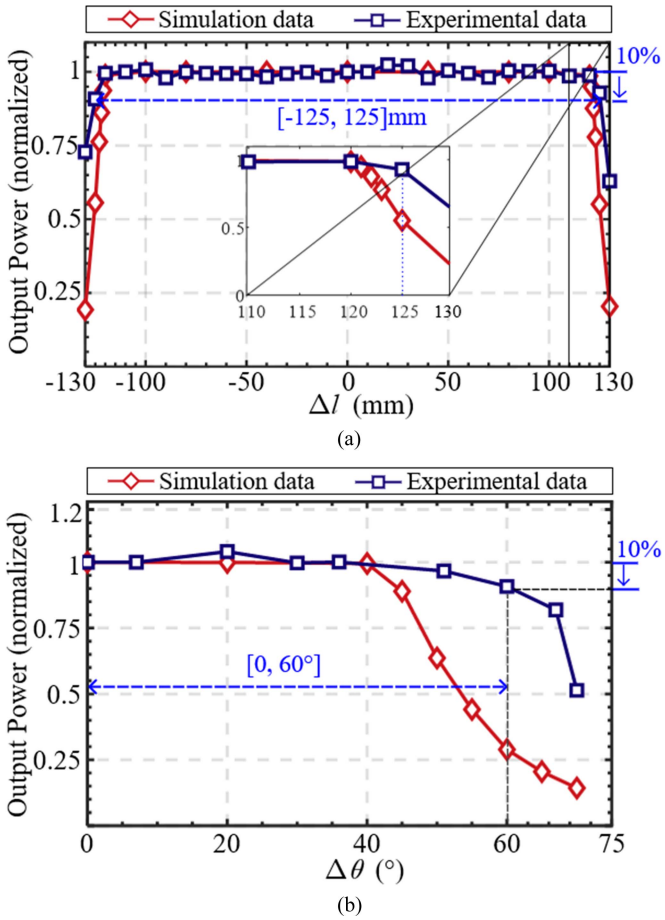

Fig. 21. Simulation and experimental results of (a) horizontal and (b) rotational misalignment (1/4 circle).

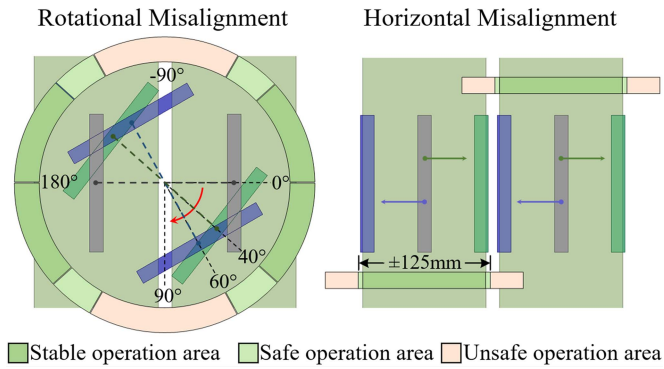

Fig. 22. Classification of safe charging areas during UAV misalignment.

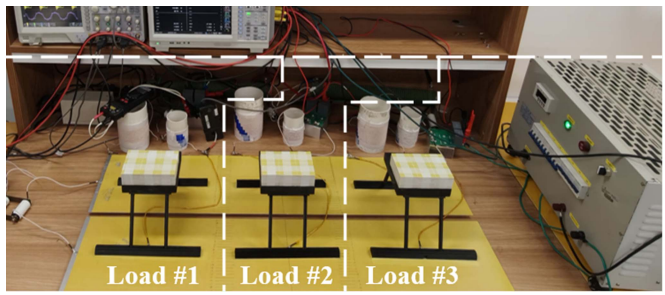

Fig. 23. Experimental platform for multiload experiment.

of the transmitter plates, maintaining stable output power and transfer efficiency. Beyond $\Delta\theta > 40°$, both output power and efficiency exhibit gradual decline, with a sharp decrease occurring after $\Delta\theta > 65°$. Using the same 10% output power deviation threshold, the experimentally validated rotational misalignment tolerance is $[0,\ 60°]$. Leveraging the central symmetry of the plate geometry, this tolerance can be extended to $[-180°,\ -120°]\cup[-60°,\ 60°]\cup[120°,\ 180°]$.

3) Safe Operating Area Classification: To provide clearer operational guidelines, the receiver plate misalignment is classified based on output power variation levels: the angular range maintaining essentially stable output power is defined as the stable operating area, regions with $\leq$10% power reduction constitute the safe operating area, and remaining areas are categorized as the unsafe operating zone. The classification results are presented in Fig. 22. A power reduction threshold of $\leq$10% defines the system's acceptable operational criteria, thereby establishing both the stable operation area and safe operation area as equivalent to its misalignment tolerance range. Notably, the experimental platform was intentionally detuned from the ZPA state to achieve ZVS for the inverter. This detuning reduces the sensitivity of I_{out} to variations in C_{S}, resulting in experimentally measured misalignment tolerance that exceeds theoretical predictions.

D. Energy Efficiency of Multiload System

To validate the multiload power transfer performance of the proposed UAVs-CWC system, a multiload prototype system was constructed, as shown in Fig. 23. This prototype retains all original components except for replacing the programmable electronic load in Fig. 18 with ripple resistors and expanding the load count to simulate simultaneous charging scenarios for multiple UAVs.

Experimental measurements of the system's total energy transfer efficiency were systematically conducted under varying load quantities. The acquired data from Table III were rigorously applied to the theoretical framework established in Section III-A to compute the system's predicted energy transfer efficiency. It should be specifically noted that the computational result derived from (29) corresponds to ac–ac efficiency. To enable direct comparison with experimental measurements, the calculated theoretical ac–ac efficiency was strategically converted to dc–dc efficiency through the application of component efficiency coefficients: 98% for inverter operation and 96% for rectifier operation. This comprehensive set of efficiency characteristics, encompassing both empirical and theoretical results, is collectively presented in Fig. 24.

As observed in Fig. 24(a), the theoretical and experimental values of system efficiency demonstrate close alignment, thereby confirming the accuracy of the preceding multiload

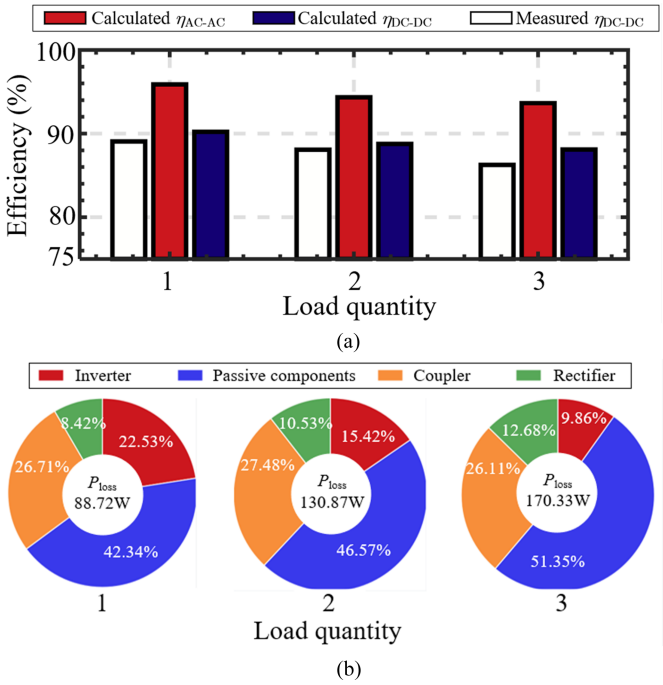

Fig. 24. (a) Efficiency and (b) loss distribution of the multiload system versus number of loads.

efficiency analysis. Simultaneously, the system maintains consistently high energy transfer efficiency levels even as the load quantity increases from one to three units. This performance characteristic conclusively verifies the system's capability to provide simultaneous charging for multiple UAVs without significant efficiency degradation.

Furthermore, loss distribution analysis across varying load counts was performed following the methodology in reference [37]. The results in Fig. 24(b) demonstrate that losses in passive components (resonant inductors and capacitors) and couplers consistently constitute the vast majority of total losses, with their proportion exhibiting an increasing trend as the number of loads rises.

Another fact is that the equivalent internal resistance of UAV lithium batteries changes during the charging process, which means that multiple loads being charged simultaneously are highly likely to have unequal values. For this reason, multiple unbalanced load charging experiments were conducted. The theoretical and measured values of the system's energy transfer efficiency under these operating conditions are presented in Fig. 25, where the numbers in the parentheses on the abscissa represent the three actual load resistance values used in each experiment. It should be noted that this experiment was carried out at a power level lower than the rated power; therefore, the measured efficiency is only used for horizontal comparison under different load conditions and cannot fully reflect the system's performance. Analysis of this figure shows that the overall energy transfer efficiency of the system is affected by unbalanced loads, but it can still maintain a relatively high level overall.

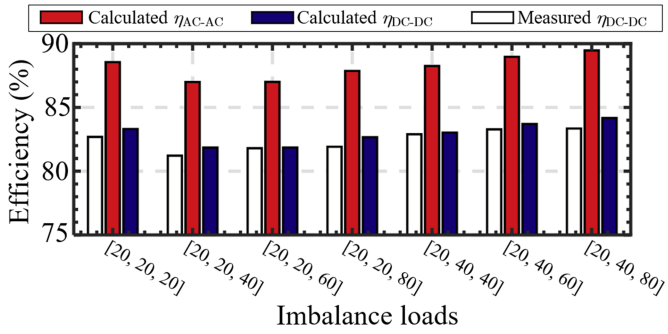

Fig. 25. Multiload system efficiency versus Imbalance loads.

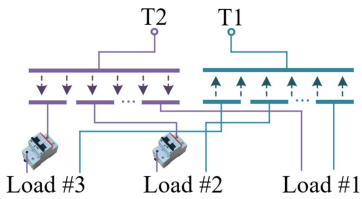

Fig. 26. Circuit breaker interconnection scheme.

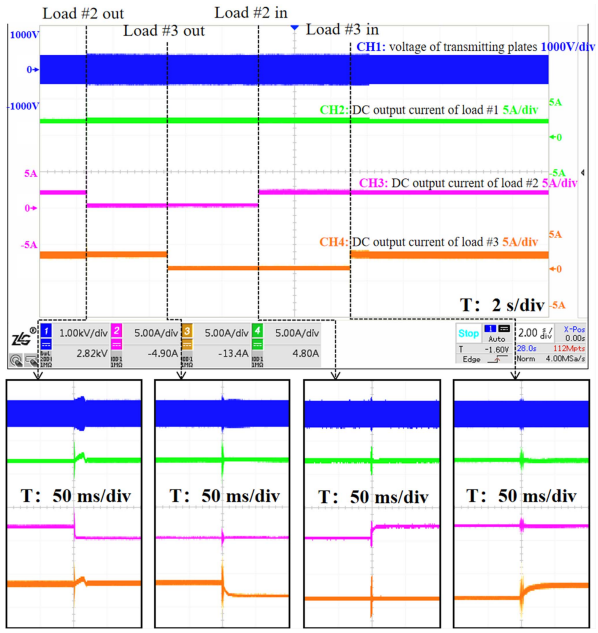

Fig. 27. Waveforms of the multiload dynamic switching experiment.

E. Multiload Dynamic Switching Experiment

To verify the load decoupling performance of the UAVs-CWC system, circuit breakers were connected in series within the power loops of Loads #2 and #3, as shown in Fig. 26. The "open→close" transition of the circuit breakers simulates the process of a UAV landing on the charging platform, while the reverse operation emulates its departure.

Following the experimental procedure outlined in Section III-B, the waveforms of $\boldsymbol{U}_{\mathrm{R}}$ and $I_{\mathrm{out\_dc}i}, (i = 1, 2, 3)$ were recorded using an oscilloscope during the entire test and are presented in Fig. 27, which reveals three key findings.

TABLE IV
COMPARISON WITH PREVIOUS WORK

Reference	WPT type	Frequency /kHz	Power /W	Efficiency /%	Structural compatibility	Horizontal misalignment tolerance	Rotational misalignment tolerance	Multiload charging capacity
[23]	IPT	85	126	91.6	★	[-80 mm, 80 mm] close-loop control	not mentioned	No
[14]	IPT	85	135.8	80	★★★	[-110 mm, 110 mm]	360° (expected)	No
[19]	IPT	500	128.2	89	★★★	[-20 mm, 20 mm]	360°	No
[10]	IPT	6780	200	89	★	[-25 mm, 25 mm]	360° (expected)	No
[37]	IPT	300	<20W	85.4%	★	[-120 mm, 120 mm]	360°	No
[38]	IPT	85	not mentioned		★	[-400 mm, 400 mm]	not mentioned	No
[26]	CPT	6780	8	77	★★★	[-20 mm, 20 mm]	90° in a circle	No
[27]	CPT	1000	100	89.4 (plate-to-plate)	★★	precise alignment with auxiliary aligning device	360°	No
[28]	CPT	500	212.1	82.5	★★★	[-100 mm, 100 mm]	360° (reconfigurable coupler)	No
This work	CPT	500	709.9	89.06	★★★	[-125 mm, 125 mm]	240° in a circle	Yes

1) All three loads operated normally with consistent charging performance at the experiment start.
2) The voltage U_R and charging current of Load #1 remained stable throughout the test. Although transient disturbances occurred during load switching events, stable operation was rapidly restored.
3) Loads #2 and #3 were effectively controlled by the circuit breakers, with their switching operations causing no interference to other loads.

Experimental results confirm that the proposed UAVs-CWC system exhibits excellent load decoupling capability, demonstrating strong suitability for UAV swarm charging applications.

F. Comparative Analysis With Prior Work

A performance comparison between the proposed UAVs-CWC system and recent related studies is summarized in Table IV. Note that due to space constraints, this table selectively presents representative works based on WPT type and coupler configuration to objectively demonstrate the advancements of the proposed system in UAV wireless charging.

1) Power and Efficiency Perspective: The proposed system achieves the highest output power (709.9 W) among all referenced studies, satisfying diverse UAV charging power requirements. Its dc–dc efficiency (89.06%) ranks highest in CPT-based UAV charging systems and surpasses most IPT-based solutions, being only slightly lower than [23].

2) Structural Compatibility: The proposed coupler demonstrates superior structural compatibility compared to [10], [23], [37], [38], and [27], supports more landing gear types than [19], and ranks among the best implementations while maintaining lightweight advantages.

3) Misalignment Tolerance: Without closed-loop control or auxiliary alignment devices, the system achieves exceptional horizontal misalignment tolerance. Under a 10% output power variation threshold, its performance rivals [37]. For rotational misalignment, it exhibits competitive tolerance without requiring complex position detection or switching strategies inherent to reconfigurable couplers.

4) Multiload Charging Capacity: The system's key innovation lies in its scalability and operational flexibility, enabling simultaneous charging for variable numbers of loads – a capability absent in prior works.

In summary, the UAVs-CWC system delivers multidrone wireless charging via a single transmitter, combining wide power range, high efficiency, robust load decoupling, and exceptional misalignment tolerance. These advancements significantly enhance flexibility and cost-effectiveness for UAV swarm operations.

VI. CONCLUSION

This article proposes a capacitive wireless charging system for UAVs that can simultaneously charge multiple UAVs using a single transmitter-side setup (power supply, inverter, and resonant network). The SIMO electric field coupler fully utilizes the landing pad and UAV landing gear to maximize the effective coupling area, exhibiting excellent structural adaptability. Targeted optimization significantly enhances its misalignment tolerance. The proposed LCLC-CLL resonant network achieves constant current output, load decoupling, and load-adaptive ZPA on the transmitter side. Experimental results demonstrate that the system achieves peak performance metrics of 709.9 W output power and 89.06% transmission efficiency under single-load operation. The operational tolerance spans horizontal misalignment within $[-125\ \text{mm}, 125\ \text{mm}]$ and rotational misalignment up to 240° in a circle. The system exhibits robust multiload adaptability, sustaining high energy transfer efficiency during both load quantity variations and multiload imbalance conditions, while demonstrating superior load-decoupling capability. In summary, the proposed UAVs-CWC system represents a creative application of multiload CPT technology in UAV charging, providing an ideal solution for UAV swarm charging.

Nonetheless, there remain issues to be resolved based on the aforementioned research. The variation in the equivalent internal resistance of lithium batteries during charging and the randomness of load quantity affect the stability of the system's ZVS state and overall energy transfer efficiency. Thus, the collaborative control and efficiency optimization of multiload systems under large-scale load fluctuations will constitute the subsequent research focus of our team.

REFERENCES

[1] G. Sun, Q. Xu, G. Zhang, T. Qu, C. Cheng, and H. Deng, "An intelligent UAV path-planning method based on the theory of the three-dimensional subdivision of earth space," *Int. J. Geo-Inf.*, vol. 12, no. 10, Sep. 2023, Art. no. 397, doi: 10.3390/ijgi12100397.

[2] A. Mukherjee, S. Misra, and N. S. Raghuwanshi, "A survey of unmanned aerial sensing solutions in precision agriculture," *J. Netw. Comput. Appl.*, vol. 148, Dec. 2019, Art. no. 102461, doi: 10.1016/j.jnca.2019.102461.

[3] J. Yi, H. Zhang, S. Li, O. Feng, G. Zhong, and H. Liu, "Logistics UAV air route network capacity evaluation method based on traffic flow allocation," *IEEE Access*, vol. 11, pp. 63701–63713, 2023, doi: 10.1109/ACCESS.2023.3238464.

[4] J. Wu et al., "An adaptive conversion speed Q-Learning algorithm for search and rescue UAV path planning in unknown environments," *IEEE Trans. Veh. Technol.*, vol. 72, no. 12, pp. 15391–15404, Dec. 2023, doi: 10.1109/TVT.2023.3297837.

[5] H. Baek and J. Lim, "Design of future UAV-relay tactical data link for reliable UAV control and situational awareness," *IEEE Commun. Mag.*, vol. 56, no. 10, pp. 144–150, Oct. 2018, doi: 10.1109/MCOM.2018.1700259.

[6] Y. Wang, S. Yan, X. Zhou, Y. Huang, and D. W. K. Ng, "Covert communication with energy replenishment constraints in UAV networks," *IEEE Trans. Veh. Technol.*, vol. 71, no. 9, pp. 10143–10148, Sep. 2022, doi: 10.1109/TVT.2022.3178021.

[7] Y. Li et al., "Research on rectifier fault diagnosis and self-protecting for inductive power transfer system with constant-current output," *IEEE Trans. Power Electron.*, vol. 40, no. 2, pp. 3750–3769, Feb. 2025.

[8] Y. Zhang, H. Zhou, Z. Shen, R. Xie, X. Chen, and X. Mao, "An interoperable dynamic wireless charging system with stable output based on a self-adaptive two-pole receiver," *IEEE Trans. Power Electron.*, vol. 39, no. 10, pp. 11943–11947, Oct. 2024, doi: 10.1109/TPEL.2024.3409368.

[9] E. Rong, P. Sun, G. Yang, J. Xia, Z. Liu, and S. Li, "5-kW, 96.5% efficiency capacitive power transfer system with a five-plate coupler: Design and optimization," *IEEE Trans. Power Electron.*, vol. 40, no. 1, pp. 2542–2555, Jan. 2025, doi: 10.1109/TPEL.2024.3462410.

[10] J. Huang, Y. Dou, X. Huang, Z. Zhang, Z. Ouyang, and M. A. E. Andersen, "Optimization of a 6.78-MHz inductive power transfer system for unmanned aerial vehicles," *IEEE Trans. Power Electron.*, vol. 38, no. 10, pp. 11940–11952, Oct. 2023, doi: 10.1109/TPEL.2023.3299833.

[11] T. Campi, F. Dionisi, S. Cruciani, V. De Santis, M. Feliziani, and F. Maradei, "Magnetic field levels in drones equipped with Wireless Power Transfer technology," in *Proc. Asia-Pacific Int. Symp. Electromagn. Compat.*. Shenzhen, China: IEEE, May 2016, pp. 544–547. doi: 10.1109/APEMC.2016.7522793.

[12] T. Campi, S. Cruciani, F. Maradei, and M. Feliziani, "Wireless charging system integrated in a small unmanned aerial vehicle (UAV) with high tolerance to planar coil misalignment," in *Proc. Joint Int. Symp. Electromagn. Compat., Sapporo Asia-Pacific Int. Symp. Electromagn. Compat.*. Sapporo, Japan: IEEE, Jun. 2019, pp. 601–604. doi: 10.23919/EMC-Tokyo.2019.8893934.

[13] S. Aldhaher, P. D. Mitcheson, J. M. Arteaga, G. Kkelis, and D. C. Yates, "Light-weight wireless power transfer for mid-air charging of drones," in *Proc. 11th Eur. Conf. Antennas Propag.*. Paris, France: IEEE, Mar. 2017, pp. 336–340. doi: 10.23919/EuCAP.2017.7928799.

[14] P. Cao et al., "Embedded Lightweight Squirrel-Cage Receiver Coil for Drone Misalignment-Tolerant Wireless Charging," *IEEE Trans. Power Electron.*, vol. 38, no. 3, pp. 2884–2888, Mar. 2023, doi: 10.1109/TPEL.2022.3225307.

[15] C. Song et al., "EMI reduction methods in wireless power transfer system for drone electrical charger using tightly coupled three-phase resonant magnetic field," *IEEE Trans. Ind. Electron.*, vol. 65, no. 9, pp. 6839–6849, Sep. 2018, doi: 10.1109/TIE.2018.2793275.

[16] Z. Bie, J. Zhang, K. Song, D. Wang, and C. Zhu, "A free-rotation asymmetric magnetic coupling structure of UAV wireless charging platform with conformal pickup," *IEEE Trans. Ind. Electron.*, vol. 69, no. 10, pp. 10154–10161, Oct. 2022, doi: 10.1109/TIE.2022.3165297.

[17] C. Cai, S. Wu, M. Qin, and Z. Yang, "A novel magnetic coupler for unmanned aerial vehicle wireless charging systems," in *Proc. IEEE Int. Power Electron. Appl. Conf. Expo.*. Shenzhen, China: IEEE, Nov. 2018, pp. 1–5. doi: 10.1109/PEAC.2018.8590492.

[18] S. Wu, C. Cai, L. Jiang, J. Li, and S. Yang, "Unmanned aerial vehicle wireless charging system with orthogonal magnetic structure and position correction aid device," *IEEE Trans. Power Electron.*, vol. 36, no. 7, pp. 7564–7575, Jul. 2021, doi: 10.1109/TPEL.2020.3047384.

[19] Y. Li et al., "A New magnetic coupler with high rotational misalignment tolerance for unmanned aerial vehicles wireless charging," *IEEE Trans. Power Electron.*, vol. 37, no. 11, pp. 12986–12991, Nov. 2022, doi: 10.1109/TPEL.2022.3184335.

[20] S. Jain, A. Bharadwaj, and A. Sharma, "A mortarboard-shaped receiver antenna for drone wireless charging to achieve an outspread misalignment tolerance towards imperfect landing," *IEEE Trans. Veh. Technol.*, vol. 74, no. 1, pp. 61–73, Jan. 2025, doi: 10.1109/TVT.2024.3452943.

[21] S. Pang, J. Xu, Z. Xie, J. Lu, H. Li, and X. Li, "Lightweight UAV's wireless power transfer system for constant current charging without secondary feedback control," *IEEE Trans. Veh. Technol.*, vol. 72, no. 12, pp. 15611–15621, Dec. 2023, doi: 10.1109/TVT.2023.3297632.

[22] C. Cai, J. Wang, H. Nie, P. Zhang, Z. Lin, and Y.-G. Zhou, "Effective-configuration WPT systems for drones charging area extension featuring quasi-uniform magnetic coupling," *IEEE Trans. Transp. Electrificatio*, vol. 6, no. 3, pp. 920–934, Sep. 2020, doi: 10.1109/TTE.2020.2995733.

[23] Z. Li, J. He, Y. Huo, M. Ban, Y. Liu, and J. Liu, "High-Misalignment tolerance and output adjustable wireless charging system via detuned series–series compensated reconfigurable transmission channels," *IEEE Trans. Power Electron.*, vol. 38, no. 10, pp. 11786–11801, Oct. 2023, doi: 10.1109/TPEL.2023.3281721.

[24] W. Zhou, D. Tang, Z. Chen, R. Mai, and Z. He, "Nonisolation model and load virtual-grounding design method for capacitive power transfer system with asymmetric four-plate coupling interface," *IEEE J. Emerg. Sel. Topics Power Electron.*, vol. 12, no. 1, pp. 208–218, Feb. 2024, doi: 10.1109/JESTPE.2023.3312370.

[25] W. Zhou et al., "Design and analysis of CPT system with wide-range ZVS and constant current charging operation using 6.78 MHz Class-E Power Amplifier," *IEEE J. Emerg. Sel. Topics Power Electron.*, vol. 12, no. 3, pp. 3211–3225, Jun. 2024, doi: 10.1109/JESTPE.2024.3375914.

[26] A. Muharam, T. M. Mostafa, and R. Hattori, "Design of power receiving side in wireless charging system for UAV application," in *Proc. Int. Conf. Sustain. Energy Eng. Application*. Jakarta, Indonesia: IEEE, Oct. 2017, pp. 133–139. doi: 10.1109/ICSEEA.2017.8267698.

[27] C. Park et al., "Separated circular capacitive coupler for reducing cross-coupling capacitance in drone wireless power transfer system," *IEEE Trans. Microw. Theory Techn.*, vol. 68, no. 9, pp. 3978–3985, Sep. 2020, doi: 10.1109/TMTT.2020.2989118.

[28] C. Cai, X. Liu, S. Wu, X. Chen, W. Chai, and S. Yang, "A misalignment tolerance and lightweight wireless charging system via reconfigurable capacitive coupling for unmanned aerial vehicle applications," *IEEE Trans. Power Electron.*, vol. 38, no. 1, pp. 22–26, Jan. 2023, doi: 10.1109/TPEL.2022.3198529.

[29] H. Zhang, H. Ma, B. W. Mersha, X. Zhang, and Y. Jin, "Distributed cooperative search method for multi-UAV with unstable communications," *Appl. Soft Comput.*, vol. 148, Nov. 2023, Art. no. 110592, doi: 10.1016/j.asoc.2023.110592.

[30] P. Wu, F. Xiao, H. Huang, and R. Wang, "Load balance and trajectory design in multi-UAV aided large-scale wireless rechargeable networks," *IEEE Trans. Veh. Technol.*, vol. 69, no. 11, pp. 13756–13767, Nov. 2020, doi: 10.1109/TVT.2020.3026788.

[31] K. Liu and J. Zheng, "UAV trajectory optimization for time-constrained data collection in UAV-enabled environmental monitoring systems," *IEEE Internet Things J.*, vol. 9, no. 23, pp. 24300–24314, Dec. 2022, doi: 10.1109/JIOT.2022.3189214.

[32] S. Wu, C. Cai, H. Zhang, X. Liu, and W. Chai, "A free-positioning IPT system via reconfigurable coil array transmitter for unmanned aerial vehicle applications," *IEEE Trans. Transp. Electrific.*, vol. 10, no. 4, pp. 8746–8757, Dec. 2024, doi: 10.1109/TTE.2024.3360054.

[33] B. Elst, H. Farbakhsh, A. Cloet, M. Kleemann, and B. Minnaert, "Introducing relay-repeaters for hybrid inductive-capacitive wireless power transfer," in *Proc. IEEE Wireless Power Technol. Conf. Expo*, Rome, Italy, 2025, pp. 1–5, doi: 10.1109/WPTCE62521.2025.11062151.

[34] M. Liao et al., "UAV fleet charging on telecom towers with differential capacitive wireless power transfer," *IEEE Trans. Power Electron.*, vol. 40, no. 4, pp. 6370–6384, Apr. 2025, doi: 10.1109/TPEL.2024.3520915.

[35] W. Liu, B. Luo, X. He, Z. Wang, and R. Mai, "Analysis of compensation topology with constant-voltage/current output for multiple loads capacitive power transfer system," *CSEE J. Power Energy Syst.*, vol. 11, no. 2, pp. 802–814, Mar. 2025, doi: 10.17775/CSEEJPES.2021.07100.

[36] Z. Liu, Y. Su, Y. Zhao, A. P. Hu, and X. Dai, "Capacitive power transfer system with double T-type resonant network for mobile devices charging/supply," *IEEE Trans. Power Electron.*, vol. 37, no. 2, pp. 2394–2403, Feb. 2022, doi: 10.1109/TPEL.2021.3105406.

[37] C. Cai et al., "Multi-state voltage balancing of UAV's cell string: A reconfigurable WPT based multiport hybrid charging approach," *IEEE Trans. Ind. Electron.*, vol. 72, no. 1, pp. 266–277, Jan. 2025, doi: 10.1109/TIE.2024.3401190.

[38] M. Xue, Y. Guo, W. Xu, Y. Gao, and S. Qiu, "Design and optimization of wide-coupling nested magnetic coupling mechanism for UAV wireless power transfer," *IEEE Trans. Power Electron.*, vol. 40, no. 8, pp. 11849–11862, Aug. 2025, doi: 10.1109/TPEL.2024.3455354.

Xiaochen Zhang was born in Qingdao, China, in 1996. He received the B.E. degree in electrical engineering and automation from Shanghai University of Electric Power, Shanghai, China, in 2019, and the M.E. degree in electrical engineering in 2022 from Naval University of Engineering, Wuhan, China, where he is currently working toward the Ph.D. degree in electrical engineering.

His current research interests include capacitive power transfer technology and its applications.

Pan Sun was born in Zibo, China in 1986. He received the B.S., M.S., and Ph.D. degrees in electrical engineering from the School of Electrical Engineering, Naval University of Engineering, Wuhan, China, in 2009, 2015, and 2022, respectively.

In 2015, he was with the School of Electrical Engineering, Naval University of Engineering as an Associate Professor. He has authored more than 70 papers, with more than 30 being published in SCI and EI journals such as IEEE Transactions and other prestigious publications.

Dr. Sun has successively led the National Key Research and Development Program, the National Natural Science Foundation, and other research projects. He was honored with 5 provincial and ministerial awards for scientific and technological progress, as well as teaching achievement awards. His research interests include wireless power transfer, the design of new transformers, special motors, and their control.

Enguo Rong (Member, IEEE) received the B.S. degree in electrical engineering and the M.S. degree in power electronics from Kunming University of Science and Technology (KUST), Kunming, China, in 2016 and 2019, respectively, and the Ph.D. degree in electrical engineering with Naval University of Engineering, Wuhan, China, in 2024.

Since 2025, he has been with the Faculty of Electric Power Engineering, KUST, as a Special-Term Associate Professor. From 2019 to 2021, he was the CEO of Kunming Minya Technology Company Ltd., a company focused on the development of high-power converters. His research interests include high-frequency dc–dc converters and wireless power transfer systems.

Dr. Rong was the recipient of the Grand Prize Award from IEEE International Future Energy Challenge in 2017.

Gang Yang received the B.S. and M.S. degrees in electrical engineering in 2014 and 2021, respectively, from Naval University of Engineering (NUE), Wuhan, China, where he is currently working toward the Ph.D. degree in electrical engineering.

In 2019, he was with the School of Electrical Engineering, NUE, as a Lecturer. His research interests include capacitive wireless power transfer and the testability of electrical equipment.

Sisi Chang received the B.E. degree in communication engineering from the College of Electronics Engineering, Naval University of Engineering, Wuhan, China, in 2018 and the M.E. degree in control engineering from the College of Electrical Engineering, Naval University of Engineering, in 2024. She is currently working toward the Ph.D. degree in electrical engineering from the Naval University of Engineering. Her research direction focusses on wireless power transfer.

Qijun Deng received the B.S and M.Sc. degrees in mechanical engineering from Wuhan University, Wuhan, China, in 1999 and 2002, respectively, and the Ph.D. degree in computer application technology from Wuhan University, Wuhan, China, in 2005.

In Jun. 2005, he was with the Department of Automation (which now is merged into School of Electrical Engineering and Automation), Wuhan University, where he is currently a Professor. From 2013 to 2014, he was a visiting scholar with New York University Tandon School of Engineering. His research interests include wireless power transfer, distribution automation, and electrical power informatics.